JGR Space Physics

RESEARCH ARTICLE
10.1029/2019JA027031

A Simulation of the Field-Aligned Plasma Transport in the Plasmaspheric Plume During the 2015 St. Patrick's Day Storm

Zheng Qiao[1,2], **Zhigang Yuan**[1], **and Jiannan Tu**[2]

[1]School of Electronic Information, Wuhan University, Wuhan, China, [2]Space Science Laboratory and Physics Department, University of Massachusetts Lowell, Lowell, MA, USA

Abstract In this paper, based on a calculated open $\mathbf{E} \times \mathbf{B}$ convection passage of a flux tube with subauroral polarization streams (SAPS) electric field involved, we use the Dynamic Fluid-Kinetic model to simulate the transport of major ion species (H^+, He^+, and O^+) along magnetic field line (field-aligned) within the flux tube during the 2015 St. Patrick's Day storm. The drift trajectory is confirmed to be quite realistic based on observations and empirical models, meanwhile, the foot print of flux tube is initiated from subauroral latitudes toward polar latitudes along this drift pass. The Dynamic Fluid-Kinetic simulation displays interesting temporal evolution of the field-aligned plasma distribution at subauroral latitudes: The storm-enhanced density region continuously provides upward ion flux filling into plasmasphere, but the equatorial mass loading in plasmaspheric plume increases at first and then decreases. Further analyses found that the SAPS particularly impact the field-aligned transport of O^+ particles from ionosphere to plasmasphere but have much less effect on H^+ and He^+ particles at subauroral latitudes, which causes significant enhancements of equatorial O^+ density. The results show that the SAPS have significant effects on both drifting trajectory of the flux tube and associated field-aligned ion dynamics. This work reveals intimate storm time interaction between the inner magnetosphere and ionosphere which may affect the dynamics in outer magnetosphere or even at magnetopause with flux tube convection.

Key Points:

- We conduct a DyFK simulation on the field-aligned cold plasma transport during a super storm with SAPS effects incorporated
- The SAPS have significant impacts on the flux tube convection as well as the field-aligned ion dynamics within the flux tube at subauroral latitudes
- The enhanced intimate interaction of SAPS and inner magnetosphere-, ionosphere system may affect the dynamics in outer magnetosphere with flux tube convection

Supporting Information:

- Supporting Information S1

Correspondence to:
Z. Yuan,
y_zgang@vip.163.com

Citation:
Qiao, Z., Yuan, Z., & Tu, J. (2019). A simulation of the field-aligned plasma transport in the plasmaspheric plume during the 2015 St. Patrick's Day storm. *Journal of Geophysical Research: Space Physics*, *124*, 8617–8628. https://doi.org/10.1029/2019JA027031

Received 12 JUN 2019
Accepted 30 SEP 2019
Accepted article online 17 OCT 2019
Published online 9 NOV 2019

1. Introduction

The plasmaspheric plume and storm-enhanced density (SED) are defined as regions filled with dense and cold plasma and are associated with enhanced geomagnetic activities, particularly magnetic storms (e.g., Coster et al., 2003, 2007; Coster & Skone, 2009; Zou et al., 2013). It has been shown that SED plume and plasmaspheric plume are the ionospheric and magnetospheric manifestations of plasma structures at both low and high latitudes or at both low and high L shells (Moldwin et al., 2016, and references therein). The SED structure is considered to be the low-altitude extension of plasmaspheric plume (Foster et al., 2002; Yizengaw et al., 2008) and be related to low-to-mid latitude ionospheric convection driven by intense poleward electric field (Kelley et al., 2004). Meanwhile, the plasmapsheric plume is discovered to have significant impacts on the dynamics in the vicinity of dayside magnetopause such as the solar wind-magnetopause coupling (Borovsky & Denton, 2006, Borovsky et al., 2008) and wave-particle interactions (Yuan et al., 2012), not just on inner magnetosphere (Borovsky & Denton, 2008).

On the other hand, under geomagnetically disturbed conditions, strong poleward electric field is frequently discovered in subauroral ionosphere, which is considered to be caused by either the separation of the equatorward boundaries of the ion and electron plasma sheets or a fraction of flowing-down Region 2 field-aligned currents (FACs) from magnetosphere (e.g., Anderson et al., 2001; Heinemann et al., 1989; Yuan et al., 2017). The electric field, termed as the subauroral polarization stream (SAPS) electric field, was found to be responsible for antisunward convection of SED plume material from subauroral to auroral latitudes (Foster et al., 2007) in addition to severe effects on the formation of plasmaspheric plume (Goldstein et al., 2003). The interaction of plasmaspheric plume and SED plume involving SAPS effects has been put forward as the research focus of storm time solar wind-magnetosphere-ionosphere-thermosphere coupling in the last decade. Observational studies discovered that the dayside midlatitude to high-latitude convection of SED not only affects the dayside middle latitude ionosphere such as uplift F layer (Yuan et al., 2009), field-aligned ion flow (Zou et al., 2014), and energetic particle precipitation (Yuan et al., 2011) but also has profound impacts on midnight polar ionosphere through two-cell convection in polar region (Yuan et al., 2008). Zhang et al. (2013) reported direct observations of the full evolution of ionized patches convecting through polar cap to nightside during storm time, arising from intense mid-high latitude convection of both ionosphere and magnetosphere. Then Foster et al. (2014) conducted a case study about storm time plasmasphere-ionosphere evolution, showing an integrated flow loop of ionospheric plasma at middle and high latitudes. The observations revealed the intimate connection between SAPS and magnetosphere-ionosphere coupling under geomagnetically disturbed conditions with solid proof. However, it is still very difficult to explore continuous evolution of the coupling dynamics based on simultaneous observations, which requires additional techniques.

In recent years, numerical models have been developed to analyze storm time dynamics in the multiway coupling among the solar-wind, magnetosphere, ionosphere, and thermosphere such as the plasma sources and the evolution of SED plume during storm time by Global Ionosphere Thermosphere Model (GITM) simulations (Zou & Ridley, 2016) and the global response of ionosphere and inner magnetosphere to a geomagnetic storm based on SAMI3-RCM simulation (Huba & Sazykin, 2014). What is more, Wang et al. (2012) demonstrated prominent SAPS impacts on Ionosphere-Thermosphere coupling system under geomagnetically disturb conditions using SAPS-driven TIEGCM simulations, followed by a simulation work which illustrates the evolution of SAPS and how SAPS affect the coupled magnetosphere-ionosphere-thermosphere system during a super storm based on LFM-TIEGCM-RCM model (Lin et al., 2019). But almost all of these models primarily aim to explore a global scale evolution without including the effects of flux tube convection. Wang et al. (2015) have developed a Dynamic Fluid-Kinetic (DyFK) model to simulate field-aligned (along the magnetic field line) plasma transport between the ionosphere and plasmasphere as well as the dynamics within a drifting closed flux tube. Through a drift trajectory along the plasmaspheric drainage plume toward dayside magnetopause, DyFK simulations are able to reveal distinguished mass loading of plasmaspheric plasma in the vicinity of dayside magnetopause which affects the solar wind-magnetosphere coupling dynamics, and to show significantly enhanced effects of the wave-particle interaction on field-aligned plasma density distribution (Wang et al., 2016).

However, Wang et al. (2016) focus on field-aligned plasma transport in the outer plasmaspheric drainage plume (high *L shells*) due to enhanced magnetospheric convection, which is beyond the latitudinal range of SAPS and neglects the contribution from middle latitudes. As noted above, the SAPS have been found to be closely related to erosion of the plasmasphere, generation of the SED plume and sunward convection of the SED material. It implies that SAPS may affect plasma transport and energy exchange processes in the complex mid-latitude to high-latitude magnetosphere-ionosphere coupling during storm time, which further changes the dynamics in outer magnetosphere or even in solar wind-magnetosphere coupling through flux tube convection. In order to have a comprehensive understanding of the magnetosphere-ionosphere coupling process especially during storm time, it is necessary to obtain more detailed investigations on field-aligned plasma dynamics along flux tubes with SAPS effects incorporated.

The 2015 St. Patrick's Day storm is the strongest one over the 24th solar cycle, which has been reported by a lot of studies (e.g., Zhang et al., 2017, and references therein) such as evolutions of the SED Plume associated with SAPS (Heine et al., 2017; Krall et al., 2017), global magnetospheric responses with plasmaspheric Plume emerging (Goldstein et al., 2017), and Ionosphere-Thermosphere coupling under the influences of SAPS (Guo et al., 2018). In the present study, we simulate a drift pass of a single closed flux tube during this super storm, under the influence from E×B drift including SAPS electric field. The drift trajectory is confirmed to be quite realistic from the comparison with observations meanwhile the SED structure and plasmaspheric plume are field-aligned coupled along the flux tube. Based on the realistic drift trajectory, the DyFK simulations are able to provide field-aligned redistribution as well as dynamics of multiple ion species (H^+, He^+, and O^+) in the plumes. If the flux tube convects more cold ions from plasmasphere to outer magnetosphere, the dynamics in the vicinity of magnetopause such as localized wave-particle interaction and reconnection rate might be significantly changed (e.g., André et al., 2016; Borovsky et al., 2008). Therefore, the equatorial mass loading including the contribution of SAPS at subauroral latitudes will be greatly helpful to understand storm time magnetosphere-ionosphere coupling process. In the next section, we describe the occupied numerical models in this study. Section 3 presents the DyFK simulation results as well as discussion. Section 4 summarizes the findings of this simulation work.

2. Simulation Method

In the present study, we consider ionospheric and plasmaspheric ion transport along a closed flux tube. We neglect curvature and gradient drift and only consider **E** × **B** drift of the flux tube for such low energy ionospheric and plasmaspheric ions. Goldstein et al. (2005) developed a Kp-dependent magnetospheric model of SAPS potential motivated by the research interest of the SAPS effect arising from Region 2 FACs flowing down into the subauroral ionosphere, which illustrates tremendous change of equatorial SAPS flow channels under geomagnetically disturbed conditions. Therefore, we combine the E5D magnetospheric convection electric potential model (McIlwain, 1986), corotation electric field, and G05 magnetospheric SAPS electric potential model (Goldstein et al., 2005) to calculate the drifting trajectory of the flux tube.

The DyFK model couples Field Line Interhemispheric Plasma (FLIP) model and Generalized Semi-Kinetic (GSK) model with an overlapped region in 800- to 1,100-km altitude range along a closed flux tube. Detailed descriptions of the model are given by Wang et al. (2015). The DyFK model is able to provide field-aligned dynamics (distributions of density, velocity and pitch angle) of multiple ion species (O^+, H^+, and He^+) along the flux tube when convecting in three-dimensional space. In DyFK model, the equations for GSK domain region are described as below (Wang et al., 2015):

$$\frac{ds}{dt} = v_{\|} + (\boldsymbol{U}_c \cdot \nabla_{\perp}) s \tag{1}$$

$$\frac{dv_{\|}}{dt} = \frac{q_i}{m_i} E_{\|} - \mathbf{g} \cdot \widehat{b} - \frac{\mu_i}{m_i} \frac{\partial B}{\partial s} - \boldsymbol{U}_c \cdot \left\{ \frac{\partial \widehat{b}}{\partial t} + \left[\left(-\widehat{b} v_{\|} + U_c \right) \cdot \nabla \right] \widehat{b} \right\} \tag{2}$$

$$\frac{d\mu_i}{dt} = \frac{d}{dt} \left(\frac{m_i v_{\perp}^2}{2B} \right) = \left[\frac{\partial}{\partial t} + \left(-\widehat{b} v_{\|} + U_c \right) \cdot \nabla \right] \left(\frac{m_i v_{\perp}^2}{2B} \right) = 0 \tag{3}$$

where s is the particle position along the magnetic field line from north to south; t refers to the time; $v_{\|}$ is the velocity antiparallel to the magnetic field line; $\mathbf{U}_\mathrm{c}$ is the drift velocity of the flux tube at position s perpendicular to the magnetic field; $v_{\perp}$ is the gyro-speed; q_i and m_i are the electric charge and mass of a physical particle, respectively; i refers to species of ions; $\mathbf{g}$ is the gravitational acceleration; $\widehat{b} = \boldsymbol{B}/B$ is the unit vector of the static dipolar magnetic field; and μ_i is the magnetic moment. As shown on the right side of equation (2), the particles are subjected to ambipolar electric field force, gravitational force, mirror force, and centrifugal force from left to right, respectively.

About the ambipolar electric field term, the model given by Mitchell et al. (1992) is adopted in the DyFK model:

$$E_{\|} = \frac{1}{S_t} \sum_j q_j \left\{ \frac{\partial}{\partial s} \left(n_j v_{j\|}^2 \right) - \frac{n_j v_{j\|}^2}{B} \frac{\partial B}{\partial s} + \frac{g n_j}{s^2} + \frac{\partial J}{\partial t} \frac{1}{A} + \frac{k_B}{m_j} \left[\frac{\partial \left(n_j T_{j\|} \right)}{\partial s} - \frac{n_j \left(T_{j\|} - T_{j\perp} \right)}{B} \frac{\partial B}{\partial s} \right] \right\} \tag{4}$$

where $S_t = \sum_j n_j e^2 / m_j$ running all ion species (O^+, H^+, and He^+) and electrons; s is the arc length along the magnetic field line in reference to the 800-km altitude in the northern hemisphere; A is cross-sectional area of the flux tube varying with B^{-1}; e is the electron charge; n_j and $v_{j\|}$ are the number density and parallel bulk velocity of species j; q_i is the electrical charge; J is the FAC; $T_{j\|}$ and $T_{j\perp}$ are the parallel and perpendicular temperatures, respectively; and k_B is the Boltzmann constant.

In addition, here the electrons are treated as fluid. The density and velocity of electrons are derived from the quasi-neutrality and parallel current-free conditions. The electron temperature is assumed to be isotropic and derived by the model provided by Titheridge (1998) as follows:

$$T_e(h) = T_0 \left[1 + \Psi(h) \frac{G_0}{T_0} \left(\frac{h_{eq} - h_0}{R_0^2} - \frac{h_{eq} - h}{R_h^2} \right) \right]^{2/7} \tag{5}$$

where

$$\Psi(h) = \frac{0.05}{2L{-}R_0}\left[88 + log\frac{h}{h_0}\left(10.5{-}log\frac{h}{h_0}\right)\right] \tag{6}$$

and h is the altitude, $R_h = 1 + \frac{h}{R_E}$, $R_0 = 1 + \frac{h_0}{R_E}$, $h_{eq} = (L-1)R_E$, and R_E is the radius of the Earth. Subscript 0 denotes values at the reference height $h_0 = 400$ km. The electron temperature T_0 and its gradient G_0 are given by the least squares fits to observations. As shown in equation (3), the mirror force term in DyFK model is calculated by the conservation of magnetic momentum. About the centrifugal force term, in the orthogonal curvilinear dipolar coordinates $Ø$, q, and p (right-handed system adopted from Rasmussen et al., 1993), the centrifugal force could be derived from the equatorial drifting velocity of the flux tube:

$$F_{cf} = U_{r\text{-}eq}v_{\parallel}\frac{3sin^4\theta(1+cos^2\theta)}{r(1+3cos^2\theta)^2} + U^2_{Ø\text{-}eq}\frac{3cos\ \theta sin^6\theta}{r(1+3cos^2\theta)^{1/2}} + U^2_{r\text{-}eq}\frac{6cos\ \theta sin^6\theta(1+cos^2\theta)}{r(1+3cos^2\theta)^{5/2}} \tag{7}$$

where θ is the colatitude and $U_{r\text{ - }eq}$ and $U_{\varnothing\text{ - }eq}$ represent relative drifting velocities on magnetic equatorial plane, respectively.

3. Simulations and Discussion

As shown in the top panel in Figure 1d, on 17 March 2015, the intensification of the magnetic storm lasted from 1200 UT to 2300 UT. The Dst index first increased then continuously decreased and reached a minimum of −220 nT while the Kp index as well as the Ap index increased around 1200 UT then remained at high levels, implying a super storm.

3.1. Flux Tube Drift Trajectory

Figures 1a to 1c display how SAPS electric field affected the magnetospheric convection system under elevated geomagnetic activities (left panels for Kp=4.0 and right panels for Kp=7.7), including the effects of corotation electric field. As shown in Figure 1 row (c), due to prominent enhancements of duskside sunward flows of SAPS (right panel of row (b)), which added to magnetospheric convection (right panel of row (a)), the original closed passages in the inner magnetosphere turned into open (that is drifting toward the magnetopause) ones near dusk side (right panel of row (c)). The SAPS significantly affect the flux tube drift and thus may have important influences on storm time evolution of SED and plasmaspheric plumes. Therefore, in the simulation we calculate drifting trajectories by adding a SAPS potential model (Goldstein et al., 2005) to the convection and corotation as shown in Figure 1, right panel of row (c). Since the Kp index remained around 2 over 1 week before the storm day (not shown here) and SAPS is more likely to appear under Kp>4 (Foster & Vo, 2002), we assumed that at 1600 UT the Kp index increased from 4.0 to 7.7 as a step function. Thereafter, the trajectory was derived from actual solar wind/IMF data and geomagnetic conditions.

Figure 2a shows the calculated drift trajectories of flux tube on magnetic equatorial plane based on magnetic indexes (Kp index and Dst index) and solar wind/IMF data. The red solid line and red dashed line denote the drift orbits under Kp=7.7 and Kp=4.0 from the same start point A (3.122 Re), respectively. Concerning wide differences of the drifting velocities under different geomagnetic conditions, we calculated the trajectory under Kp=4.0 (7 hr) for a longer time duration than under Kp=7.7 (3 hr) to see whether the first passage would have a chance to reach the dayside magnetopause. As shown in Figure 2a, in contrast with the open passage under Kp=7.7, which reached dayside magnetopause, the passage under Kp=4.0 extended to the night side. The discrepancy of two trajectories revealed that the SAPS electric field “pushed” the drifting flux tube changing from a closed $\mathbf{E} \times \mathbf{B}$ drift orbit to an open one. Points A, B and C, D refer to the start point, the two azimuthally “turning around” points, the end point of the open passage. Based on the time variations of velocity (described in Text S1 of supporting information), we conclude that the SAPS severely reduce the azimuthal velocity of flux tube then result in its first turning-around motion, while the second turning-around motion is dominated by convection electric field.

Figure 2b presents snapshots of global GPS total electron content (TEC) map, with 350-km projection of the open passage using the magnetospheric magnetic field model T96 (Tsyganenko, 1995). Determinations of vertical TEC have been binned in 2°×5° latitude/longitude bins and color coded between 0 and 2 $\log_{10}$(TECU; one total electron content unit [TECU]=10^{16} electrons m^{-2}; Coster et al., 2003). The scattered projections from points C to D are attributed to dominant two-cell convection at high latitudes. As shown by

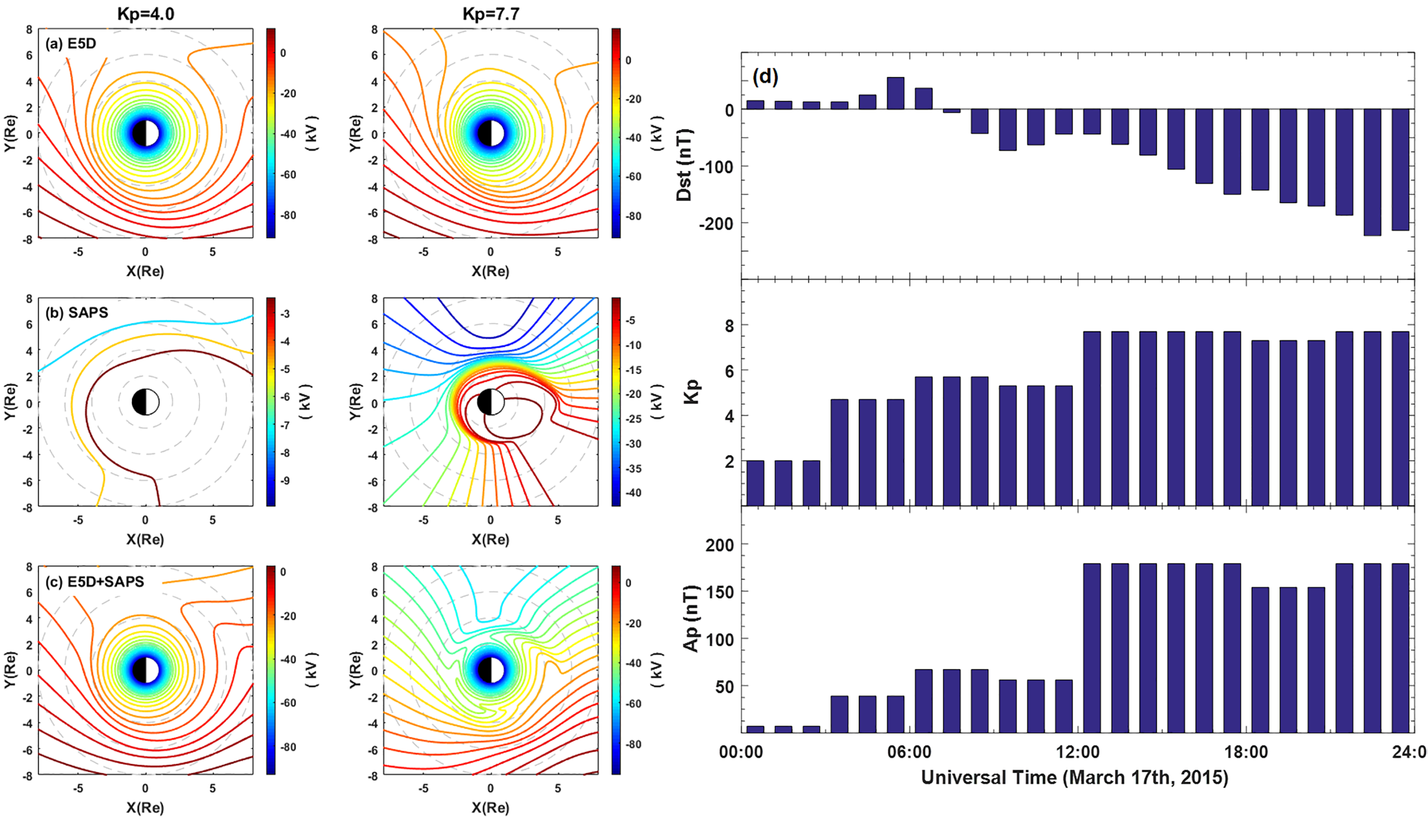

Figure 1. Equatorial potential including the effects of corotation electric field in SM coordinate shown in row (a) E5D model with 2.5-kV spacing, row (b) SAPS model with 4-kV spacing, and row (c) SAPS added to E5D with 4-kV spacing. In rows (a)–(c) left panels for Kp=4.0 and right panels for Kp=7.7, respectively. (d) Geomagnetic indices on 17 March 2015.

black solid points in Figure 2b, the footprint of the flux tube at 350-km altitude remained inside the SED structure from start to finish.

3.2. DyFK Simulation Results

The simulation was initialed by running the FLIP model with a closed flux tube corotating with the Earth at L=3.122 Re (~55.5° invariant latitude) starting from magnetic local noon time under Kp=4.0, with solar activity index F10.7 set at 113.5. In the FLIP simulation, the flux tube density reaches equilibrium over a period of 1 week, which provides a flux tube with full and stable field-aligned plasma distribution same as previous studies (Wang et al., 2016; Zeng & Horwitz, 2008). A more detailed description of preparations for the initial condition has been given by Wang et al. (2016). In the semikinetic domain GSK region (above 800 km in both hemisphere), the initial velocity distribution functions of ions (H^+, He^+, and O^+) were assumed to be drifting Maxwellian. The density and bulk velocity distributions of electrons were derived based on quasi-neutral assumption. Based on the magnetopause model established by Shue et al. (1998), the flux tube arrived at the dayside magnetopause at 1900 UT. In this study, we focus on period from 1600 to 1855 UT.

Based on the open convection passage (the one which extends toward dayside magnetopause) in Figure 2a, the DyFK model was employed to simulate dynamics within the closed flux tube, of which the foot passed through the SED region in the North hemisphere. As shown in Figure 2c, in comparison with empirical model established by Sheeley et al. (2001), the simulated equatorial electron density remains above the scopes of plasmasphere and plasmaspheric trough density ranges, implying high plasma density distribution inside the equatorial portion of the flux tube. Also, comparisons between the open passage and the Plasmapause Test Particle (PTP) simulation based on Van Allen Probe observations (Goldstein et al., 2014) showed that the equatorial portion of the flux tube was drifting within plasmaspheric plume from beginning to end, which are shown in Text S2 of supporting information. Combining panels (a), (b), and (c) in Figure 2,

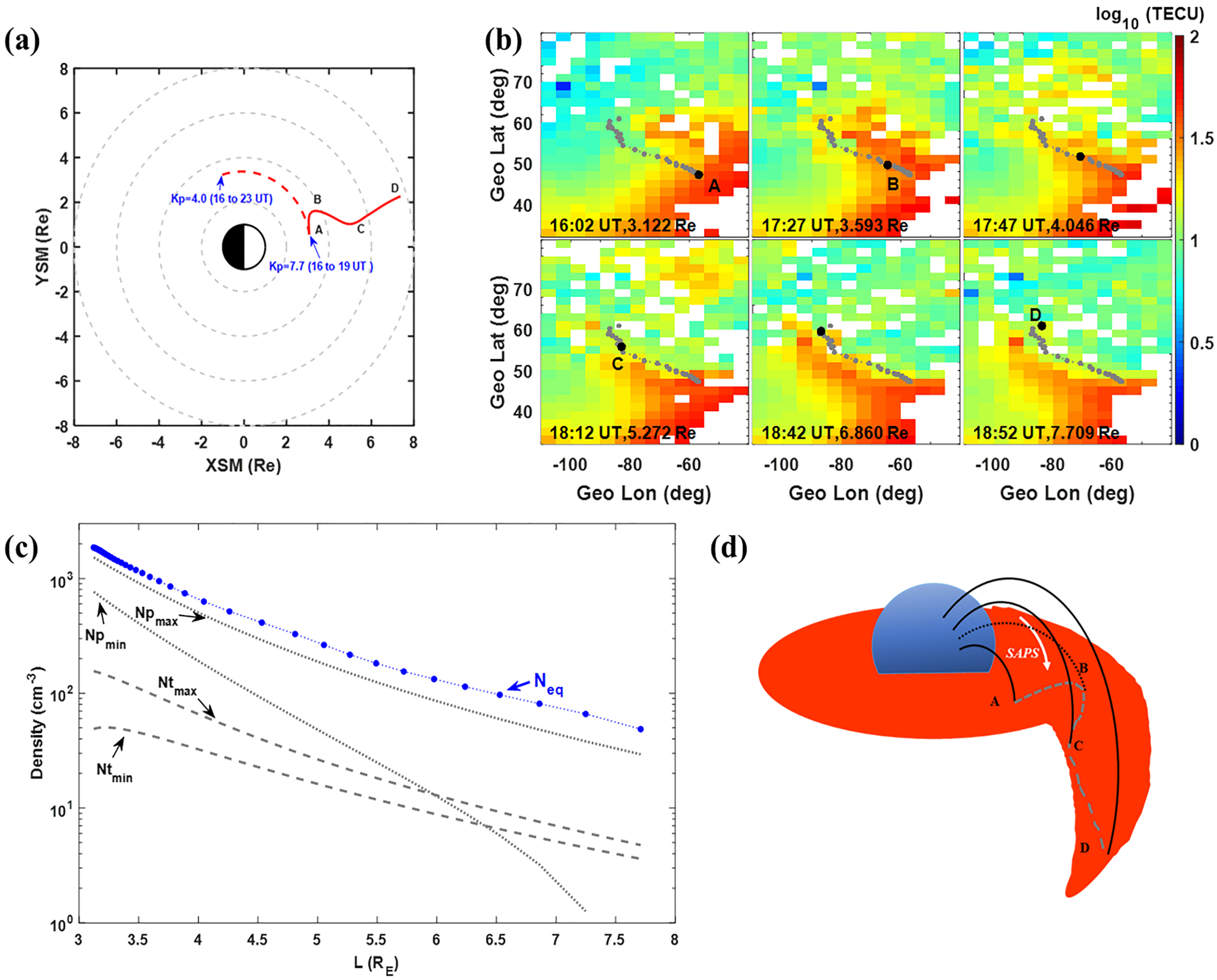

Figure 2. (a) Flux tube drifting trajectories on equatorial plane in SM coordinate system under Kp=4.0 and Kp=7.7, respectively. (b) 350-km altitude projection of the open passage on the global total electron content (TEC) map. The grey dotted lines with solid point in each snapshot represent projections of the open passage and the black solid point represents the projection at present. Labels A, B, C, and D correspond to those in panel (a). (c) Comparisons between the simulated equatorial electron density (blue dotted line with solid points) and the empirical model. Np_{max}, Np_{min}, Nt_{max}, and Nt_{min} denote the maximum density in plasmasphere, the minimum density in plasmasphere, the maximum density in trough, and the minimum density in trough, provided by Sheeley et al. (2001), respectively. (d) A three-dimensional schematic description of the flux tube drifting along the open passage referring to (a). The white arrow refers to the flow of subauroral polarization streams (SAPS).

we construct a dynamic framework about the cause-effect mechanisms between SAPS electric field and evolution of the plasmasphere-ionosphere plume during the 2015 St. Patrick's Day storm. As shown in Figure 2d, at first the SAPS electric field "pushed" the flux tube out of closed $\mathbf{E} \times \mathbf{B}$ drift L shells (mark A, L= 3.122 Re) followed by azimuthal "turning around" (mark B, L=3.584 Re), then it drove the flux tube drifting toward dayside magnetopause including second time "turning around" (mark C, L=5.209 Re) by synergistic effects with the high-latitude convection patterns.

It is well known that the ionosphere is a major plasma source for the Earth's magnetospheric plasma populations (e.g., Chappell et al., 1987; Tu et al., 2006, 2007). Observations have shown the presence of field-aligned ion upflows at F-region heights in the SED region during geomagnetic storms (Yuan et al., 2009), which may reach the magnetospheric equator along the flux tube if possessed enough initial kinetic energy. In order to obtain the field-aligned plasma transport between the plasmaspheric plume and underlying SED region in our study, as shown in Figure 3, we present the plasma flux at topside ionosphere (900 km) and at magnetospheric equator, respectively. In addition, as shown in Figure 4, we examine variations of parallel velocity

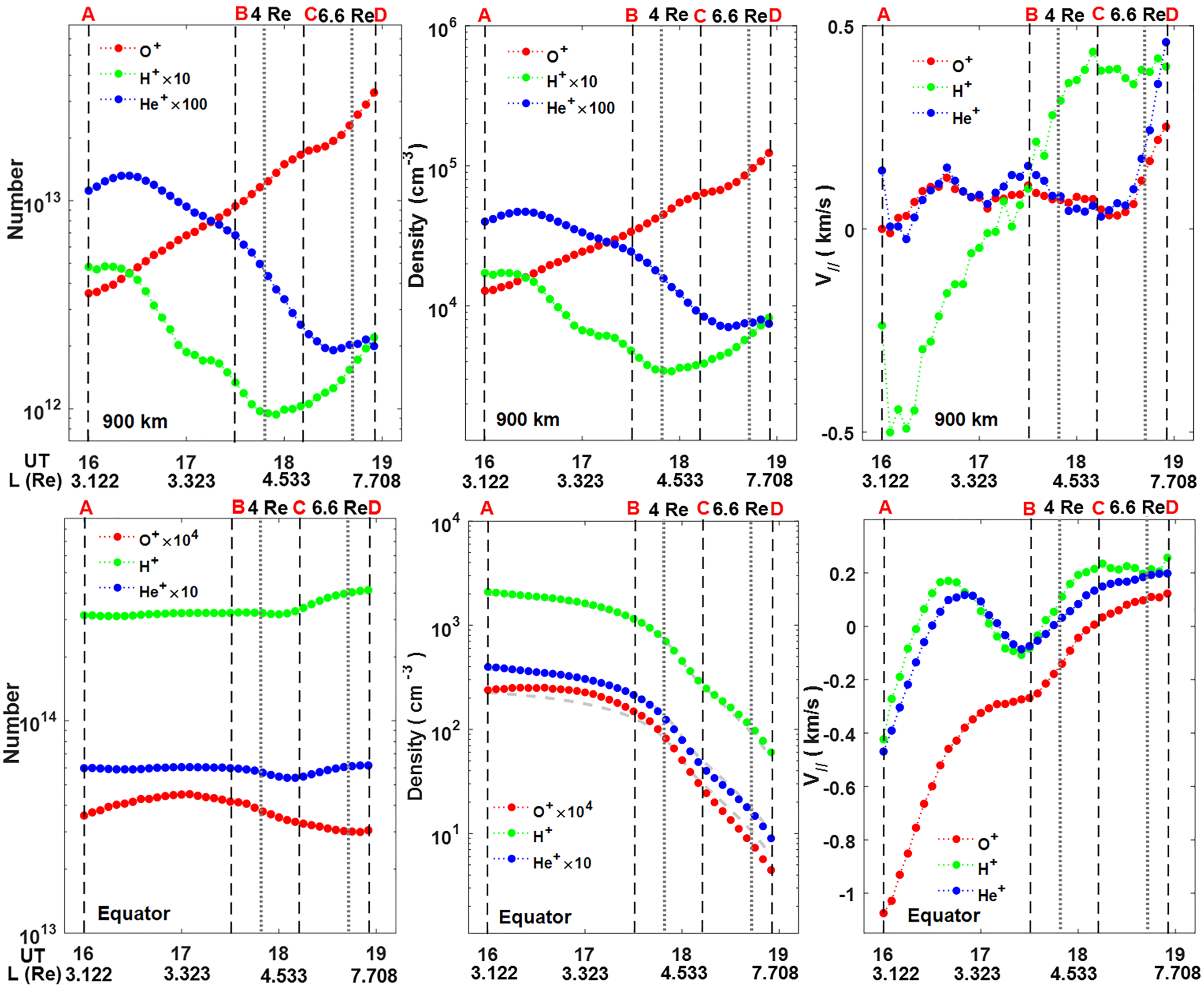

Figure 3. Variations of total count (total number of particles) in grid cell (left), density (middle) and bulk velocity (right) of different ion species (green for H^+, blue for He^+, and red for O^+) at 900-km altitude in north hemisphere (upper panels) and magnetic equator (bottom panels). Labels A, B, C, and D corresponding to points in Figure 2a.

distributions along the flux tube ((a) to (c)) as well as the density (d) and parallel bulk velocity distributions (e) for different ion species (H^+, He^+, and O^+) so as to further understand the field-aligned plasma redistributions.

In the simulation, the cell width of grid is about 30 km around 900-km altitude and hundreds of kilometers at magnetospheric equator along the flux tube, respectively. In the panel of equatorial densities (middle panel in bottom row of Figure 3), the grey dashed lines represent variations with L^{-4} corresponding to the volume change of the flux tube. If the mass flux is conservative, the equatorial densities are expected to vary as the dashed lines. The total counts in Figure 3 (left panels) are derived by multiplying the density with corresponding volume of grid cell.

As shown in Figure 3 (right panel in upper row), after the sudden increase of geomagnetic activity, at ionospheric heights the ions (H^+, He^+, and O^+) are mainly bounded by gravitational force hence move downward (the parallel bulk velocity is upward positive in the North Hemisphere) at the beginning (label A). Due to the heavy mass, the velocity of O^+ particles is relatively small. Then the density of dominant O^+ in ionosphere

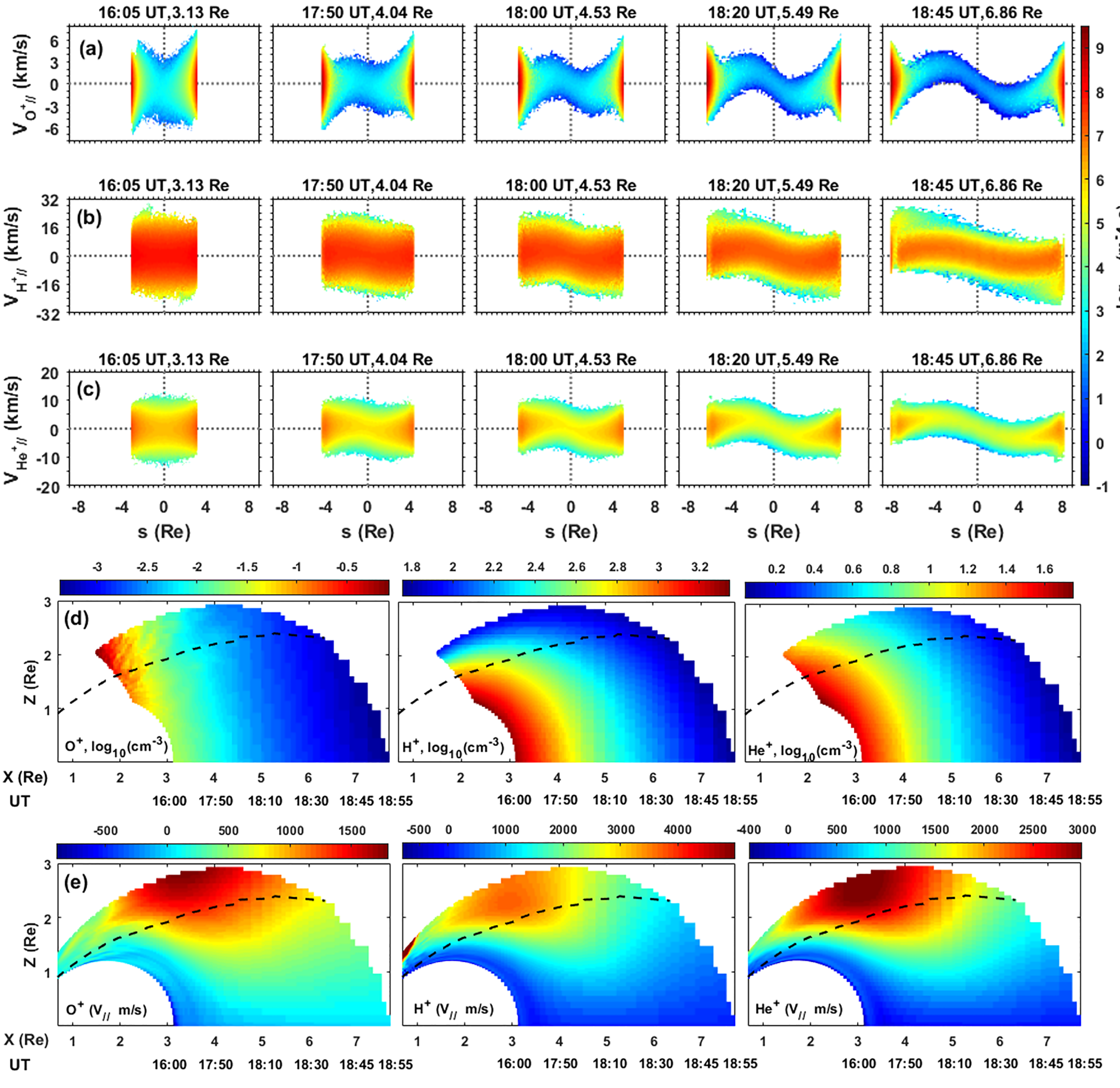

Figure 4. (a–c) Parallel velocity distributions of O^+, H^+, and He^+ along the flux tube at different time epochs as well as different L shells. The particle position along the field line, s, is negative (positive) in the northern (southern) hemisphere with unit in Re. (d) Density distributions of ions (from left to right: O^+, H^+, and He^+) above 1.5 Re altitude along the magnetic field line in North Hemisphere. (e) Parallel bulk velocity distributions of ions (from left to right: O^+, H^+, and He^+) along the flux tube in North Hemisphere. The black dashed lines denote the tracks of the grid cell, which was located at 800-km altitude at the beginning. The parallel velocity is positive from north to south hemisphere.

rapidly increases and its upward bulk velocity keeps increasing until 1630 UT (3.193 Re). From then on, the ionosphere has been providing relatively stable upward O^+ flow on the order of 10^{12} $m^{-2} \cdot s^{-1}$ while the ionospheric O^+ density is increasing. Meanwhile, both the equatorial density and total count of O^+ particles remain increasing from the beginning till 1700 UT (left and middle panels in bottom row of Figure 3), associated with 30-min time delay of filling process from underlying ionosphere, corresponding to the travelling time from topside ionosphere to magnetospheric equator. The increments of O^+ density both in topside ionosphere and around magnetospheric equator provide straightforward field-aligned filling process from SED region to plasmaspheric plume within the flux tube at subauroral latitudes.

Since about 1730UT (L=3.47 Re), due to rapid growth in radial drifting velocity (shown in Figure S1 in supporting file), the flux tube convects toward higher *L-shells* with more prominent geometrical change. As a result, the ionospheric O^+ particles have to travel a much longer distance before they arrive the equator, which requires higher initial kinetic energy. On the other hand, the geometrical change comes with volume expansion of grid cells especially around the equator, which dominates the varations of equatorial O^+ density. Hence, the density of O^+ particles at equator decreases. Although the O^+ density keeps increasing in topside ionosphere (middle panel of top row in Figure 3), the O^+ particles move slowly toward the equator along the magnetic field line which could be identified in Figure 4a and left panel in Figure 4d. As the flux tube drifting toward the dayside magnetopause, the O^+ particles gain maximum parallel velocity around the altitude of 3 Re (Figure 4e), but most of them will be trapped at low-to-mid latitudes. As a result, as shown in Figure 3, after 1730 UT the equatorial total count of O^+ particles keeps decreasing (left panel in bottom row of Figure 3) while in topside ionosphere the continous O^+ upward flow exists the whole period (middle and right panels in upper row of Figure 3). Around 1800 UT, the ionospheric O^+ bulk velocity starts decreasing, which should be attributed to the synergistic effects of decreasing geomagnetic activities (Figure 1d) and downward O^+ flow from high altitudes. Although the ionospheric upflow of O^+ particles dramatically increases (up to $3.115\times10^{13}\ \mathrm{m}^{-2}\cdot\mathrm{s}^{-1}$) in the last 30 min, it is expected that most of the upward O^+ flows are yet unable to reach the equator but trapped in North hemisphere during the prominent expansion of the flux tube. It is to be noted that the ionospheric O^+ density is increasing through the whole time as the flux tube drifting toward higher latitudes, which is concluded to be closely connected to the uplift F layer (Yuan et al., 2009) and the enhanced production rate under active geomagnetic activities.

However, for the light ions (H^+ and He^+), as shown in Figures 4b and 4c, they achieve equilibrium along the flux tube very fast so that we do not see any increase in either total count or density at the equator from the beginning, which is distinctly different from O^+ particles. Till 1800 UT, as shown in Figure 3 (middle panel in bottom row), the densities of light ions show L^{-4} dependence with constant total counts at the equator. After 1800 UT, as shown in left panel in bottom row of Figure 3, the equatorial total counts of H^+ and He^+ significantly increase. Those obvious increments of light ions should be attributed to ionospheric heating effects (Schunk & Nagy, 1978) based on deployed electron temperature model (Titheridge, 1998) in DyFK model, according to the enhancements of ionospheric upward ion distributions shown in Figure 3 (right panel in upper row) and Figure 4e (left and right panels).

Since the heavy ions (O^+) show quite different behaviors from light ions (H^+ and He^+) in our simulation, we carefully analyzed the factors driving the field-aligned movement of ions based on the mathematical methodology we mentioned. In the GSK domain region of DyFK model, the ion movements are subjected to synthetic effects of forces and collisions, while among them the centrifugal force is related to the drifting velocities of the flux tube (Wang et al., 2015) and described in the above equation (7). In our study, we found that the SAPS severely reduced the azimuthal-velocity-related term in equation (7) based on Text S1 of supporting information. And the details about accelerations of O^+ and H^+ particles under major forces are provided in Text S3 of supporting information.

For heavy ions (O^+), the gravitational force overcomes the combined action of other forces which accelerate the particles, and thus dominates the movement of particles. Hence, only the O^+ particles that gain much more initial kinetic energy from underlying ionosphere would reach the equator. While for light ions (H^+ for example as we mentioned in supporting information), in comparison to the acceleration of ambipolar electric field, the impacts from gravitational force are extremely minor. As shown in Figures 4b to 4d, the light ions gain enough kinetic energy from underlying ionosphere more easily and they achieve distribution equilibrium along the flux tube in a short time.

The results show intuitionistic field-aligned filling process from SED region to plasmaspheric plume and obvious equatorial mass loading at subauroral latitudes during storm time, under the synthetic effects of SAPS electric field and more disturbed geomagnetic activities. Furthermore, the cold ions could be carried away with the moving flux tube due to its low kinetic energy, and the equatorial plasma density, mass density and cold ion concentration are crucial parameters for the efficiency of magnetic reconnection process (André et al., 2016; Brovosky & Denton, 2006; Borovsky & Denton, 2008, Borovsky et al., 2008), through which the plasma and energy transport from the solar wind into the magnetosphere (Walsh et al., 2014). Our simulation reveals that the SAPS affect not only the drifting of the flux tube but also the field-aligned plasma transport along the flux tube, which finally have impacts on the equatorial dynamics at dayside magnetopause.

4. Summary

In this study, a realistic drifting trajectory of a closed flux tube through SED plume or plasmaspheric plume region during the 2015 St. Patrick's Day storm was calculated including the SAPS effect, based on geomagnetic indices as well as the solar wind/IMF data. The corresponding field-aligned dynamics of cold plasma and cold ions (H^+, He^+, and O^+) within the flux tube was then simulated by DyFK model.

The simulations of drift trajectory have shown that when the SAPS electric field is active, it can effectively "push" the flux tube out of the closed $\mathbf{E}\times\mathbf{B}$ drift orbit into an open one at subauroral latitudes. Comparisons with observation and empirical models reveal that the flux tube will further drift into high latitude meanwhile passing through SED plume at ionospheric heights or plasmaspheric plume in magnetic equatorial plane. In general, we have presented a characteristic flux tube, which carries cold-dense plasmaspheric plasma, convects through plumes toward dayside magnetopause and participates in localized dynamic process in this study.

Although we only consider $\mathbf{E}\times\mathbf{B}$ drift effects, the DyFK simulation shows obvious field-aligned filling process from SED region to plasmaspheric plume along with slight equatorial mass loading inside the flux tube at subauroral latitudes. In addition, we derive the field-aligned density redistributions and transport dynamics of major ion species (H^+, He^+, and O^+) inside the flux tube along the open passage. The results show that, as the flux tube is drifting toward the dayside magnetopause, the light ions (H^+ and He^+) rapidly reach equilibrium along the magnetic field line within the flux tube while the heavy ions (O^+) cannot penetrate into the opposite hemisphere but "pile up" near the equator hence show distinct distributions. Further analyses demonstrate that the SAPS triggered $\mathbf{E}\times\mathbf{B}$ drift dramatically changes the field-aligned transport of heavy ions (O^+) from underlying ionosphere into plasmasphere but has less effect on light ions (H^+ and He^+), which causes the large difference in ion distributions.

Our study demonstrates the SAPS to be the pivotal role of intensive inner magnetosphere-ionosphere coupling as well as the mid-to-high latitude convection during the 2015 St. Patrick's Day super storm. Following DyFK simulation provides the field-aligned dynamics within the flux tube, which systematically reveals the communication between SED plume and plasmaspheric plume via plasma transport during storm time. This work also implies intimate connections between inner magnetosphere-ionosphere coupling and dynamics in the vicinity of dayside magnetopause under active geomagnetic conditions.

As we mentioned above, we only focused on the influences of SAPS electric field on the $\mathbf{E}\times\mathbf{B}$ drift of the flux tube and on the field-aligned cold plasma transport from SED region to the plasmaspheric plume. However, SAPS have been considered to have much more profound effects on magnetosphere-ionosphere-thermosphere coupling process (e.g., Lin et al., 2019; Wang et al., 2012; Yuan et al., 2011; Zou et al., 2014). Moreover, many studies have been conducted on ion flows and transport at high latitudes, which showed that multiple processes are involved (Tu et al., 2005; Wang et al., 2016; Yuan et al., 2012; Zeng & Horwitz, 2008). The simulations under more complicated situation will be discussed in our future work.

Acknowledgments
The authors are grateful to MIT Haystack Observatory for GPS TEC data obtained from their Madrigal data center (http://madrigal.iggcas.ac.cn/madrigal/). The Dst, Kp, Ap index data are provided by the World Data Center for geomagnetism at Kyoto University at http://wdc.kugi.kyoto-u.ac.jp. The solar wind and IMF data are provided at https://cdaweb.gsfc.nasa.gov/index.html/. This work was supported by NSF grant AGS-1702134 and the National Natural Science Foundation of China (41874194, 41521063, and 41374168). The simulation data are archived in the servicer of University of Massachusetts Lowell (https://ulcar.uml.edu/downloads.html). The authors thank Paul Song for his unconditional assistance and informative discussions about this work.

References

Anderson, P. C., Carpenter, D. L., Tsuruda, K., Mukai, T., & Rich, F. J. (2001). Multisatellite observations of rapid subauroral ion drifts (SAID). *Journal of Geophysical Research*, *106*(A12), 29,585–29,599. https://doi.org/10.1029/2001JA000128

André, M., Li, W., Toledo-Redondo, S., Khotyaintsev, Y. V., Vaivads, A., Graham, D. B., et al. (2016). Magnetic reconnection and modification of the Hall physics due to cold ions at the magnetopause. *Geophysical Research Letters*, *43*, 6705–6712. https://doi.org/10.1002/2016GL069665

Borovsky, J. E., & Denton, M. H. (2006). Effect of plasmaspheric drainage plumes on solar-wind/magnetosphere coupling. *Geophysical Research Letters*, *33*, L20101. https://doi.org/10.1029/2006GL026519

Borovsky, J. E., & Denton, M. H. (2008). A statistical look at plasmaspheric drainage plumes. *Journal of Geophysical Research*, *113*, A09221. https://doi.org/10.1029/2007JA012994

Borovsky, J. E., Hesse, M., Birn, J., & Kuznetsova, M. M. (2008). What determines the reconnection rate at the dayside magnetosphere? *Journal of Geophysical Research*, *113*, A07210. https://doi.org/10.1029/2007JA012645

Chappell, C. R., Moore, T. E., & Waite, J. H. Jr. (1987). The ionosphere as a fully adequate source of plasma for the Earth's magnetosphere. *Journal of Geophysical Research*, *92*(A6), 5896–5910. https://doi.org/10.1029/JA092iA06p05896

Coster, A., & Skone, S. (2009). Monitoring storm-enhanced density using IGS reference station data. *Journal of Geodesy*, *83*(3–4), 345–351.

Coster, A. J., Colerico, M. J., Foster, J. C., Rideout, W., & Rich, F. (2007). Longitude sector comparisons of storm enhanced density. *Geophysical Research Letters*, *34*, L18105. https://doi.org/10.1029/2007GL030682

Coster, A. J., Foster, J. C., & Erickson, P. J. (2003). Monitoring the Ionosphere with GPS. *GPS World*, *14*(5), 42–49.

Foster, J. C., Erickson, P. J., Coster, A. J., Goldstein, J., & Rich, F. J. (2002). Ionospheric signatures of plasmaspheric tails. *Geophysical Research Letters*, *29*(13), 1623. https://doi.org/10.1029/2002GL015067

Foster, J. C., Erickson, P. J., Coster, A. J., Thaller, S., Tao, J., Wygant, J. R., & Bonnell, J. W. (2014). Storm time observations of plasmasphere erosion flux in the magnetosphere and ionosphere. *Geophysical Research Letters*, *41*, 762–768. https://doi.org/10.1002/2013GL059124

Foster, J. C., Rideout, W., Sandel, B., Forrester, W. T., & Rich, F. J. (2007). On the relationship of SAPS to storm enhanced density. *Journal of Atmospheric Space Terrestrial Physics*, *69*(3), 303–313. https://doi.org/10.1016/j.jastp.2006.07.021

Foster, J. C., & Vo, H. B. (2002). Average characteristics and activity dependence of the subauroral polarization stream. *Journal of Geophysical Research*, *107*(A12), 1475. https://doi.org/10.1029/2002JA009409

Goldstein, J.,Angelopoulos, V., De Pascuale, S., Funsten, H. O., Kurth, W. S., LLera, K., et al., (2017), Cross-scale observations of the 2015 St. Patrick's day storm: THEMIS, Van Allen Probes, and TWINS,*Journal of Geophysical Research: Space Physics*, *122*, 368– 392. https://doi.org/10.1002/2016JA023173

Goldstein, J., Burch, J. L., & Sandel, B. R. (2005). Magnetospheric model of subauroral polarization stream. *Journal of Geophysical Research*, *110*, A09222. https://doi.org/10.1029/2005JA011135

Goldstein, J., De Pascuale, S., Kletzing, C., Kurth, W., Genestreti, K. J., Skoug, R. M., et al. (2014). Simulation of Van Allen Probes plasmapause encounters. *Journal of Geophysical Research: Space Physics*, *119*, 7464–7484. https://doi.org/10.1002/2014JA020252

Goldstein, J., Sandel, B. R., Hairston, M. R., & Reiff, P. H. (2003). Control of plasmaspheric dynamics by both convection and sub-auroral polarization stream. *Geophysical Research Letters*, *30*(24), 2243. https://doi.org/10.1029/2003GL018390

Guo, J.-P., Deng, Y., Zhang, D.-H., Lu, Y.,Sheng, C., & Zhang, S.-R. (2018). The effect of subauroral polarization streams onionosphere and thermosphere during the 2015 St. Patrick's Day storm: Global ionosphere-thermosphere model simulations. *Journal of Geophysical Research: Space Physics*, *123*, 2241–2256. https://doi.org/10.1002/2017JA024781

Heine, T. R. P., Moldwin, M. B., & Zou, S. (2017). Small-scale structure of the mid-latitude storm enhanced density plume duringthe March 17, 2015 St. Patrick's Day storm, *Journal of Geophysical Research: Space Physics*, *122*, 3665– 3677. https://doi.org/10.1002/2016JA022965

Heinemann, N. C., Gussenhoven, M. S., Hardy, D. A., Rich, F. J., & Yeh, H.-C. (1989). Electron/ion precipitation differences in relation to Region 2 field aligned currents. *Journal of Geophysical Research*, *94*, 13,593–13,600. https://doi.org/10.1029/JA094iA10p13593

Huba, J. D., & Sazykin, S. (2014). Storm time ionosphere and plasmasphere structuring: SAMI3-RCM simulation of the 31 March 2001 geomagnetic storm. *Geophysical Research Letters*, *41*, 8208–8214. https://doi.org/10.1002/2014GL062110

Kelley, M. C., Vlasov, M. N., Foster, J. C., & Coster, A. J. (2004). A quantitative explanation for the phenomenon known as stormenhanced density. *Geophysical Research Letters*, *31*, L19809. https://doi.org/10.1029/2004GL020875

Krall, J., Huba, J. D., & Sazykin, S. (2017). Erosion of the plasmasphere during a storm, *Journal of Geophysical Research: Space Physics*, *122*, 9320–9328. https://doi.org/10.1002/2017JA024450

Lin, D., Wang, W., Scales, W. A., Pham, K., Liu, J., Zhang, B., et al. (2019). SAPS in the 17 March 2013 storm event: Initial results from the coupled magnetosphere-ionosphere-thermosphere model. *Journal of Geophysical Research: Space Physics*, *124*, 6212–6225. https://doi.org/10.1029/2019JA026698

McIlwain, C. (1986). A Kp dependent equatorial electric field model. *Advances in Space Research*, *6*(3), 187–197. https://doi.org/10.1016/0273-1177(86)90331

Mitchell, H. G., Ganguli, S. B., & Palmadesso, P. J. (1992). Diodelike response of high-latitude plasma in magnetosphere-ionosphere coupling in the presence of field-aligned currents. *Journal of Geophysical Research*, *97*(A8), 12,045–12,056. https://doi.org/10.1029/92JA00796

Moldwin, M. B., Zou, S., & Heine, T. (2016). The story of plumes: The development of a new conceptual framework for understanding magnetosphere and ionosphere coupling. *Annales de Geophysique*, *34*, 1243–1253. https://doi.org/10.5194/angeo-34-1243-2016

Rasmussen, C. E., Guiter, S. M., & Thomas, S. G. (1993). A two-dimensional model of the plasmasphere: Refilling time constants. *Planetary and Space Science*, *41*(1), 35–43. https://doi.org/10.1016/0032-0633(93)90015-T

Schunk, R. W., & Nagy, A. F. (1978). Electron temperatures in the F region of the ionosphere: Theory and observations. *Reviews of Geophysics*, *16*(3), 355. https://doi.org/10.1029/RG016i003p00355

Sheeley, B. W., Moldwin, M. B., Rassoul, H. K., & Anderson, R. R. (2001). An empirical plasmasphere and trough density model: CRRES observations. *Journal of Geophysical Research*, *106*(A11), 25631–25641. https://doi.org/10.1029/2000JA000286

Shue, J.-H., Song, P., Russell, C. T., Steinberg, J. T., Chao, J. K., Zastenker, G., et al. (1998). Magnetopause location under extreme solar wind conditions. *Journal of Geophysical Research*, *103*(A8), 17691–17700. https://doi.org/10.1029/98JA01103-5

Titheridge, J. E. (1998). Temperatures in the upper ionosphere and plasmasphere. *Journal of Geophysical Research*, *103*(A2), 2261–2277. https://doi.org/10.1029/97JA03031

Tsyganenko, N. A. (1995). Modeling the Earth's magnetospheric magnetic field confined within a realistic magnetopause. *Journal of Geophysical Research*, *100*(A4), 5599–5612. https://doi.org/10.1029/94JA03193

Tu, J., Horwitz, J. L., & Moore, T. E. (2005). Simulating the cleft ion fountain at polar perigee altitudes. *Journal of Atmospheric and Solar - Terrestrial Physics*, *67*(5), 465–477. https://doi.org/10.1016/j.jastp.2004.11.009

Tu, J., Song, P., Reinisch, B. W., & Green, J. L. (2007). Smooth electron density transition from plasmasphere to the subauroral region. *Journal of Geophysical Research*, *112*, A05227. https://doi.org/10.1029/2007JA012298

Tu, J., Song, P., Reinisch, B. W., Green, J. L., & Huang, X. (2006). Empirical specification of field-aligned plasma density profiles for plasmasphere refilling. *Journal of Geophysical Research*, *111*, A06216. https://doi.org/10.1029/2005JA011582

Walsh, B. M., Foster, J. C., Erickson, P. J., & Sibeck, D. G. (2014). Simultaneous ground- and space-based observations of the plasmaspheric plume and reconnection. *Science*, *343*(6175), 1122–1125. https://doi.org/10.1126/science.1247212

Wang, W., Talaat, E. R., Burns, A. G., Emery, B., Hsieh, S., Lei, J., & Xu, J. (2012). Thermosphere and ionosphere response to subauroral polarization streams (SAPS): Model simulations. *Journal of Geophysical Research*, *117*, A07301. https://doi.org/10.1029/2012JA017656

Wang, Y., Tu, J., & Song, P. (2015). A new Dynamic Fluid-Kinetic model for plasma transport within the plasmasphere. *Journal of Geophysical Research: Space Physics*, *120*, 8486–8502. https://doi.org/10.1002/2015JA021345

Wang, Y., Tu, J., & Song, P. (2016). Mass Loading at the magnetopause through the plasmaspheric plume. *Journal of Geophysical Research: Space Physics*, *121*, 9501–9516. https://doi.org/10.1002/2016JA022395

Yizengaw, E., Dewar, J., MacNeil, J., Moldwin, M. B., Galvan, D., Sanny, J., et al. (2008). The occurrence of ionospheric signatures of plasmaspheric plumes over different longitudinal sectors. *Journal of Geophysical Research*, *113*, A08318. https://doi.org/10.1029/2007JA012925

Yuan, Z., Qiao, Z., Li, H., Huang, S., Wang, D., Yu, X., & Yu, T. (2017). Subauroral polarization stream on the outer boundary of the ring current during an energetic ion injection event. *Journal of Geophysical Research: Space Physics*, *122*, 4837–4845. https://doi.org/10.1002/2016JA023570

Yuan, Z., Xiong, Y., Pang, Y., Zhou, M., Deng, X., Trotignon, J. G., et al. (2012). Wave-particle interaction in a plasmaspheric plume observed by a Cluster satellite. *Journal of Geophysical Research*, *117*, A03205. https://doi.org/10.1029/2011JA017152

Yuan, Z., Zhao, L., Xiong, Y., Deng, X., & Wang, J. (2011). Energetic particle precipitation and the influence on the sub-ionosphere in the SED plume during a super geomagnetic storm. *Journal of Geophysical Research*, *116*, A09317. https://doi.org/10.1029/2011JA016821

Yuan, Z.-G., Deng, X.-H., & Wang, J.-F. (2008). DMSP/GPS observations of intense ion upflow in the midnight polar ionosphere associated with the SED plume during a super geomagnetic storm. *Geophysical Research Letters*, *35*, L19110. https://doi.org/10.1029/2008GL035462

Yuan, Z.-G., Deng, X.-H., Zhang, S.-R., Wan, W.-X., & Reinisch, B. W. (2009). F region behavior in the SED plume during a geomagnetic superstorm: A case study. *Journal of Geophysical Research*, *114*, A08303. https://doi.org/10.1029/2008JA013841

Zeng, W., & Horwitz, J. L. (2008). Storm enhanced densities (SED) as possible sources for Cleft Ion Fountain dayside ionospheric outflows. *Geophysical Research Letters*, *35*, L04103. https://doi.org/10.1029/2007GL032511

Zhang, Q. H., Zhang, B. C., Lockwood, M., Hu, H. Q., Moen, J., Ruohoniemi, J. M., et al. (2013). Direct observations of the evolution of polar cap ionization patches. *Science*, *339*(6127), 1597–1600. https://doi.org/10.1126/science.1231487

Zhang, S.-R., Zhang, Y., Wang, W., & Verkhoglyadova, O. P. (2017). Geospace system responses to the St. Patrick's Day storms in 2013 and 2015. *Journal of Geophysical Research: Space Physics*, *122*, 6901–6906. https://doi.org/10.1002/2017JA024232

Zou, S., Moldwin, M. B., Ridley, A. J., Nicolls, M. J., Coster, A. J., Thomas, E. G., & Ruohoniemi, J. M. (2014). On the generation/decay of the storm-enhanced density plumes: Role of the convection flow and field-aligned ion flow. *Journal of Geophysical Research: Space Physics*, *119*, 8543–8559. https://doi.org/10.1002/2014JA020408

Zou, S., & Ridley, A. J. (2016). Modeling of the Evolution of Storm-Enhanced Density Plume during the 24 to 25 October 2011 Geomagnetic Storm. In C. R. Chappell, R. W. Schunk, P. M. Banks, J. L. Burch, & R. M. Thorne (Eds.), *Magnetosphere-Ionosphere Coupling in the Solar System* (pp. 205–213). Hoboken, NJ, USA: John Wiley & Sons, Inc. https://doi.org/10.1002/9781119066880.ch16

Zou, S., Ridley, A. J., Moldwin, M. B., Nicolls, M. J., Coster, A. J., Thomas, E. G., & Ruohoniemi, J. M. (2013). Multi-instrument observations of SED during 24–25 October 2011 storm: Implications for SED formation processes. *Journal of Geophysical Research: Space Physics*, *118*, 7798–7809. https://doi.org/10.1002/2013JA018860